# Self-Driven Photodetectors Based on Flexible Silicon Nanowires Array Surface-Passivated With Tin-Based Perovskites

Zhenheng Zhang, Shengyi Yang, Zhenhua Ge, Haiyuan Xin, Ying Wang, Yurong Jiang, and Bingsuo Zou

Abstract—Self-driven photodetectors based on flexible silicon nanowire (Si-NW) array have attracted widespread research interests since they can continuously operate without external bias. However, their practical performances are limited due to the high density of intrinsic defects introduced by the chemical etching procedure for the Si-NWs. To address this issue, first ultrathin silicon wafers are etched with a metal-assisted chemical etching method, then flexible Si-NWs are obtained, and finally, a high-performance self-driven photodetector Si/[Si-NWs/FASnBr$_3$]/MoO$_3$/Au, in which Si-NWs are surface passivated with FASnBr$_3$ nanocrystals, is presented. As a result, the responsivity and specific detectivity of the self-driven photodetector reach 0.694 A/W and 2.9 × 10^{13} Jones, respectively, under 0.8 μW/cm^2 980 nm illumination at zero bias, with a rising time of 58.552 ms and a falling time of 43.729 ms. The enhanced device performance is mainly due to the improved surface passivating effect on the silicon nanowire surfaces by FASnBr$_3$ nanocrystals. Thus, it provides an efficient method to passivate the surfaces of silicon nanowires, and it is a promising method to enhance the performances of self-driven Si-NW-based photodetectors.

Index Terms—Flexible silicon nanowire (Si-NW) array, self-driven photodetectors, surface passivating, tin-based perovskites.
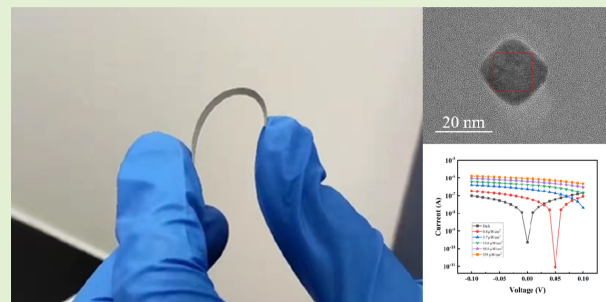
I. INTRODUCTION

NOWADAYS, photodetectors based on semiconductor nanostructures have shown a plenty of potential applications in detecting optical signals, such as in automatic manufacture, chemical/biological measurement, image sensing, military survey, and optical communication. Self-driven photodetectors [1], which can operate without external bias, further broaden the applications of photodetectors. It is unde-

niable that the vast majority of high-performance self-driven photodetectors are prepared on 1-D nanowire arrays, such as ZnO nanorods array [2], Si nanowire array [3], [4], and CdS nanorod array [5], [6]. However, the necessary high responsivity and quick response speed of photodetectors, and the ability to detect a wide range of wavelengths are also key factors. Therefore, the self-driven photodetectors based on Si-NWs have attracted the attention of many researchers. Hong et al. [7] fabricated a self-driven CuO/Si-NW broadband photodetector for the first time, and the responsivity and specific detectivity of the photodetector reached 0.064 mA/W and 7.6 × 10^8 Jones under 550 mW/cm^2 1064 nm illumination, respectively. However, the fact cannot be ignored that most of these Si-NWs were obtained by the Ag-assisted chemical etching approach. The Si-NWs obtained by this method have a large number of defects, and the existence of these defects severely limits the device performance of Si-NW-based photodetectors.

To address these issues, perovskite nanomaterials were used to passivate the surface of Si-NWs due to their high carriers' mobility, long carriers' diffusion distance, and high absorption of incident light [8]. Liu et al. [9] prepared the Si-NWs/perovskite core-shell nano-heterojunction NIR photodiode by depositing a Cs-doped FAPbI$_3$ layer onto the surface of the vertical Si-NWs. Also, the responsivity and the specific

detectivity reached 14.86 mA/W and 2.04×10^{10} Jones at zero bias, respectively. In addition, PbS nanocrystals have also been used in the surface passivation of Si-NWs. Xu et al. [10] have successfully prepared NIR/SWIR dual-band photodetectors based on Si-NWs/PbS heterojunction, and the responsivity and the specific detectivity of the photodetector in the SWIR band are 290 mA/W and 2.4×10^{10} Jones, respectively. However, among these proposed strategies, the use of semiconductor materials containing toxic elements, such as lead, will further limit the application scenarios of the above self-driven photodetectors. In contrast, the usage of nontoxic tin-based perovskites, which can be synthesized through hot injection [11] and ligand-assisted reprecipitation [12], makes them promising candidates for surface passivation of the Si-NWs.

For tin-based perovskites, the two 5s electrons of Tin(II) are active and they are easy to be lost because the inert pair effect derived from the shrinkage of the lanthanides is not present, so Tin(II) is more easily to be oxidized to Tin(IV) [13]. It is undeniable that the quality of tin-based perovskites synthesized by hot injection is high. However, the corresponding synthesis process is too complicated due to the high temperature and nitrogen environment required for the reaction process. In addition, due to the high sensitivity of the tin-based perovskites itself to oxygen, as a result, a substantial degradation of the quality of tin-based perovskites occurs. Dai et al. [12] synthesized the $FASnI_3$ nanocrystals with different particle sizes in the gloves, and they also observed a significant redshift for the absorption spectrum of the nanocrystals with increasing their particle size. Therefore, the synthesis of high-quality tin-based perovskite in a glove box is very important for high-performance self-driven photodetectors.

In this work, first the ultrathin silicon wafers are etched, and then, the flexible Si-NWs are obtained. A high-performance self-driven photodetector based on these flexible Si-NWs is presented after the Si-NWs are surface passivated with $FASnBr_3$ nanocrystals. As a result, the responsivity and the specific detectivity of the self-driven photodetector Si/[Si-NWs/FASnBr$_3$]/MoO$_3$/Au are 0.183 A/W and 7.65×10^{12} Jones, respectively, under 0.9 μW/cm^2 405 nm illumination at zero bias. These two parameters increase to 0.694 A/W and 2.90×10^{13} Jones, respectively, under 0.8 μW/cm^2 980 nm illumination at zero bias. The rising/falling time of the self-driven photodetector Si/[Si-NWs/FASnBr$_3$]/MoO$_3$/Au is reduced from the original 92.418/58.984 ms for photodetector without surface passivated active layer to 25.823/28.016 ms for photodetector with surface passivated active layer under 405 nm illumination, while the response time of the photodetector under 980 nm irradiation is reduced from the original 202.84/251.71 to 58.552/43.729 ms. Finally, the underlying mechanisms for the enhanced performance of the self-driven photodetector are discussed.
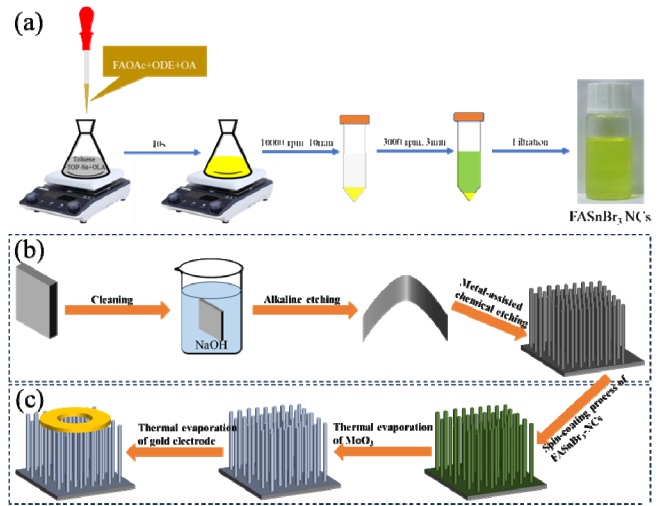

Fig. 1. (a) Synthesis procedures of FASnBr$_3$ nanocrystals. (b) Preparation procedure for the flexible Si-NWs. (c) Preparation procedure for the photodetector Si/[Si-NWs/FASnBr$_3$]/MoO$_3$/Au.

II. EXPERIMENTAL SECTION

The chemical reagents used in our experiments are of analytical grade and they are used as received. Silver nitrate (AgNO$_3$, 99%) is purchased from Beijing Tongguang Fine Chemicals Company. Hydrogen peroxide (H$_2$O$_2$, 30%) and nitric acid (HNO$_3$, 65%–68%) are purchased from Xilong Scientific Company Ltd. Formamidinium acetate (FAOAc, 99%), trioctylphosphine (TOP, 90%), oleyamine (OLA, 80%–90%), and oleic acid (OA, 99%) are purchased from Shanghai Macklin Biochemical Company Ltd. 1-Octadecene (ODE, 95%) is purchased from Meryer (Shanghai) Biochemical Technology Company Ltd. Hydrofluoric acid (HF, 40%), sodium hydroxide (NaOH, 98%), and Tin(II)-bromide (SnBr$_2$, 99%) are purchased from Shanghai Aladdin Biochemical Technology Company Ltd. Toluene (C$_7$H$_8$, 99.8%) is purchased from Tianjin Fuyu Fine Chemical Company Ltd. Molybdenum trioxides (MoO$_3$, 99.5%) are purchased from Aladdin Industrial Corporation. Dimethylformamides are purchased from Shanghai Macklin Biochemical Company Ltd. Silicon wafers are bought from Kaihua Lijing Electronics Company Ltd.

The FASnBr$_3$ nanocrystals are synthesized by injecting formamidinium oleate precursor solution into a solution of SnBr$_2$ precursor, and the above synthesis reaction is carried out in a glove box, as shown in Fig. 1(a). First, 0.083 g of formamidine acetate (FAOAc), 1 mL of 1-octadecene (ODE), and 2 mL of oleic acid (OA) are mixed at 130 °C by continuously stirring until all of FAOAc reacted with OA to yield a clear formamidinium oleate solution. Then, 0.5570 g of SnBr$_2$ is completely dissolved in 2 mL of trioctylphosphine (TOP) by continuously stirring overnight at room temperature to prepare the SnBr$_2$-TOP solution; 30 mL of toluene is heated to 80 °C in a 50-mL flask on a hot plate, followed by adding 200 μL of oleyamine (OLA) and 2 mL of SnBr$_2$-TOP solution and stirred them to form the SnBr$_2$ precursor. Finally, formamidinium oleate solution is rapidly injected into the reaction flask. After the crude solution is cooled down to room temperature, FASnBr$_3$ nanocrystals are extracted from the crude solution by centrifuging at 10 000 r/min for 10 min. After centrifugation, the supernatant solution is discarded and the precipitate is redispersed in hexane. The solution is centrifuged at 3000 r/min for 3 min to remove the aggregated
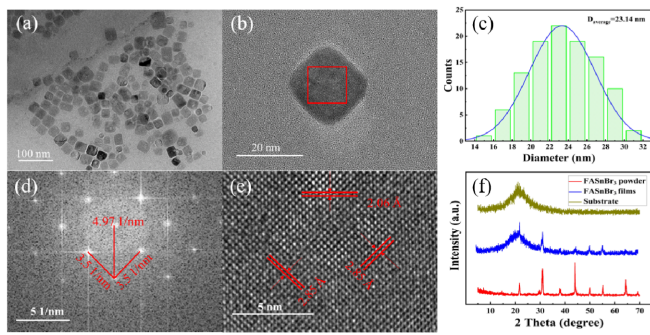
Fig. 2.	(a) TEM. (b) Diameter distribution diagram. (c) HRTEM of FASnBr$_3$ nanocrystals. (d) IFFT. (e) FFT diagram of FASnBr$_3$ nanocrystals in the red box area of (b). (f) XRD images of FASnBr$_3$ powder, FASnBr$_3$ films, and glass substrate.

Fig. 3.	(a) FTIR spectrum of FASnBr$_3$ nanocrystals. Enlarged FTIR spectrum of FASnBr$_3$ nanocrystals at wavelength for (b) 3500–3000 cm^{-1} and (c) 3000–2700 cm^{-1}.

nanocrystals, resulting in the supernatant of long-term colloidally stable solution.

In our experiments, the flexible Si-NWs are prepared by following the procedures reported [14] with a Ag-assisted chemical etching approach [15] in Fig. 1(b). The preparation procedure for self-driven photodetector Si/[Si-NWs/FASnBr$_3$]/MoO$_3$/Au is shown in Fig. 1(c). First, the flexible Si-NWs are immersed into a hybrid solution composed of 1.0 mL of HF and 10 mL of deionized water, and then, it is placed on a hot table at 45 °C for 10 min. Then, the FASnBr$_3$ nanocrystal solution is spin-coated on the flexible Si-NWs at 1000 r/min for 30 s, and then, it is annealed at 70 °C for 10 min. It is transferred into the evaporation chamber, 30 nm of MoO$_3$ is deposited at a rate of 0.1 Å/s under a high vacuum of 5 × 10^{-4} Pa, and subsequently, a 35 nm Au top electrode is thermally evaporated at a rate of 0.2 Å/s under the same vacuum condition via shadow mask. The effective illumination area on the photodetector is about 0.1256 cm^2.

III. RESULTS AND DISCUSSION

The crystallography of the as-synthesized FASnBr$_3$ nanocrystals is characterized by transmission electron microscopy (TEM), as depicted in Fig. 2(a), showing the FASnBr$_3$ nanocrystals in cube. The distribution of FASnBr$_3$ nanocrystal size is not only uniform but also no obvious agglomeration. The HRTEM of FASnBr$_3$ nanocrystals is shown in Fig. 2(b), where one can see the lattice fringe clearly. Also, one can see that the size of FASnBr$_3$ nanocrystals is 14–32 nm, and their average size is ∼23.14 nm, as shown in Fig. 2(c). After the inverse Fourier transform is applied to the area surrounded by the red box in Fig. 2(b), the clear diffraction spots can be observed in the above IFFT diagram and the spacing between the diffraction spots is 3.50, 4.97, and 3.50 1/nm, as shown in Fig. 2(d). Also, the lattice fringes can be seen clearly in the FFT diagram, and the fringe spacings are 2.85, 2.06, and 2.85 Å. Since there is no literature report on the standard pdf card of FASnBr$_3$, therefore, the above three lattice fringes and spots cannot be marked [see Fig. 2(d) and (e)] [16], [17], [18]. The XRD of the FASnBr$_3$ nanocrystal powder and film is shown in Fig. 2(f); they are slightly different from each other due to the influence of the glass substrate. However, similar diffraction peaks can be observed when the effect
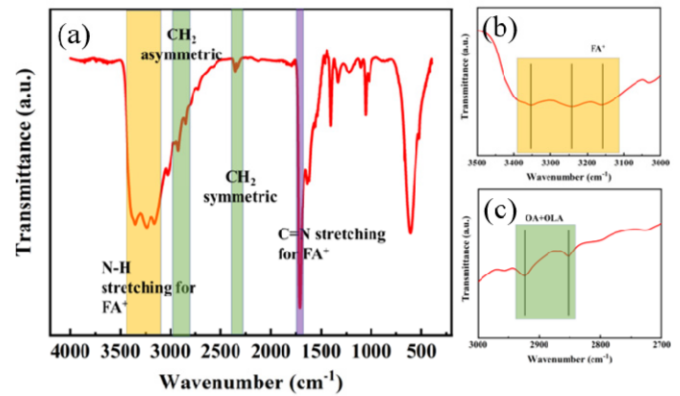
of the glass substrate is ignored, and the obvious diffraction peaks can be observed at 21.66°, 30.94°, 37.8°, 43.99°, 50.04°, 55.22°, 64.37°, and 69.16°. From the XRD of the FASnBr$_3$ nanocrystals, one can see that the interplanar spacing of the FASnBr$_3$ nanocrystals is 2.88 and 2.05 Å when 2θ is 30.94° and 43.99°, respectively. In a word, the above XRD of the FASnBr$_3$ nanocrystals is consistent with their TEM.

In order to understand the growing mechanism of FASnBr$_3$ nanocrystals, they are characterized by the FTIR spectra, as shown in Fig. 3(a). From Fig. 3(b), one can see that the vibrational peaks of N–H bond of FA$^+$ at 3357, 3270, and 3168 cm^{-1} are the vibrational peaks of the N–H bond of FA$^+$ [19], and these successive vibrational peaks are mainly formed by the interaction of FA$^+$ and Br$^-$ (N–H–B) [20]. In addition, the vibrational peak at 1715 cm^{-1} proves the presence of C=N in FA$^+$ [21], [22]. In Fig. 3(c), the vibrational peaks at 2853 and 2925 cm^{-1} are mainly associated with the symmetric and antisymmetric $^-$CH$_2$ vibrational peaks within oleic acid and oleyamine [22].

During the synthesis of FASnBr$_3$ nanocrystals, if too much oleylamine is added to the reaction solution, the color of the solution remains colorless after injecting the formamidinium oleate precursor solution into the SnBr$_2$-TOP precursor solution. This phenomenon is completely different from the change of the solution color from colorless to yellowish green as described in Section II. When excess oleylamine is injected into the SnBr$_2$-TOP precursor solution, RH^{3+} replaces FA$^+$ on the surface of FASnBr$_3$ nanocrystals and forms 2-D perovskite materials [22]. In addition, we can also see that the color of the FASnBr$_3$ nanocrystals' raw solution changes from the original yellowish green to colorless after oleylamine is poured into the synthesized FASnBr$_3$ nanocrystals' raw solution. During the synthesis of many 2-D perovskites, ammonium ions with larger ionic radii are often used to replace the A-site cation in the ABX$_3$ perovskite structure. However, the bandgap of the 2-D perovskites tends to be larger than that of the 3-D perovskites because their ionic radii are much larger than that of the A-site cation. Therefore, this phenomenon of the color changes of the FASnBr$_3$ nanocrystals' raw solution during the
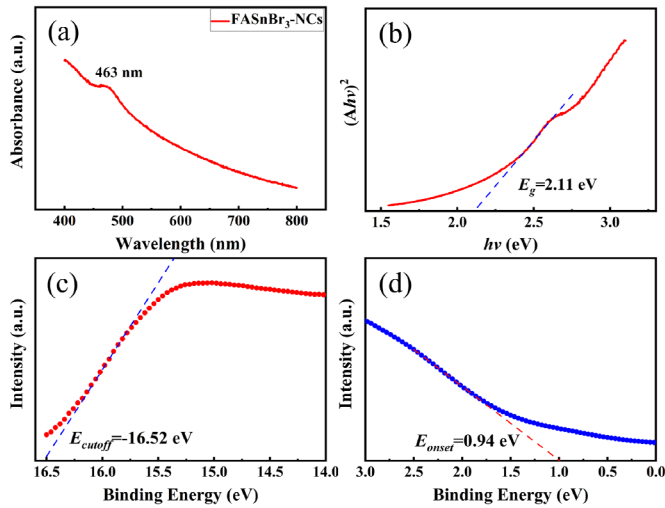
Fig. 4. (a) Absorption spectra. (b) $(Ah\nu)^2 \sim h\nu$ curve. (c) UPS spectra to the secondary electron cutoff energy. (d) Fermi energy of the FASnBr$_3$ nanocrystals film.
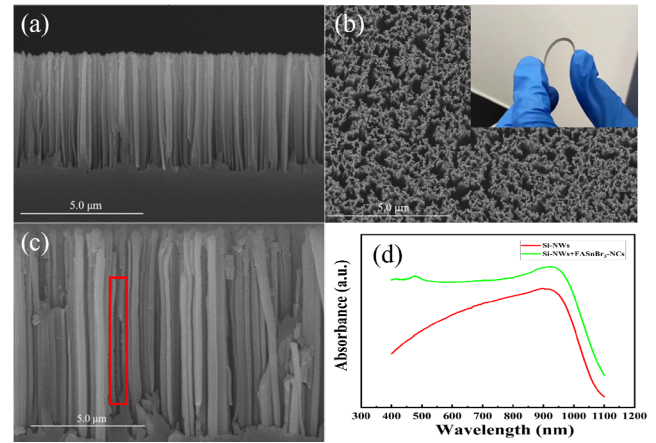

Fig. 5. (a) Side view and (b) top view of the SEM images of as-prepared flexible Si-NWs. The inset in (b) shows its corresponding plane view. (c) Magnified SEM images of the as-prepared flexible Si-NWs. (d) Absorption spectra of the Si-NWs/FASnBr$_3$-NCs bulk heterojunction and flexible Si-NWs.

synthesis of FASnBr$_3$ nanocrystals after introducing excess oleylamine can be explained.

For photodetectors, the optical properties of the active layer play a decisive role on their photodetection performance. Therefore, the absorption spectra of FASnBr$_3$ nanocrystal films by UV–visible spectrophotometer are measured, as shown in Fig. 4(a). One can see that the FASnBr$_3$ nanocrystal film has a clear absorption peak at 463 nm. The Tauc curve of the FASnBr$_3$ nanocrystals film is given in Fig. 4(b), and one can see that the bandgap of the FASnBr$_3$ nanocrystals film is ~2.11 eV. In addition, in order to find out the detailed energy band of the FASnBr$_3$ nanocrystal film, the UPS is carried out on it, as shown in Fig. 4(c) and (d). From here, one can see that the secondary electron cutoff energy of the FASnBr$_3$ nanocrystal film corresponds to $E_{cutoff} = 16.52$ eV, while the Fermi energy corresponds to $E_{onset} = 0.94$ eV, and the valence band maximum (VBM) corresponds to the HOMO level and the conduction band minimum (CBM) to the LUMO level can be obtained by the following equation [23]:

$$E_{HOMO} = h\nu - (E_{cutoff} - E_{onset}) \qquad (1)$$

$$E_{LUMO} = E_{HOMO} - E_g \qquad (2)$$

Therefore, the HOMO level is -5.64 eV, and the LUMO level is -3.53 eV for the FASnBr$_3$ nanocrystal film.

Fig. 5(a) and (b) shows the SEM images of the flexible Si-NWs, the height of the above Si-NWs is ~4.69 μm, and the diameter of the flexible Si-NWs is ~125 nm. From the inset in Fig. 5(b), the Si-NWs show good flexibility. Compared with those in Fig. 5(a), the roughness of the Si-NW surface is polished after dealing with FASnBr$_3$ nanocrystals, and some particles can be observed on the surface of the Si-NWs, especially in the region surrounded by the red box [see Fig. 5(c)]. This phenomenon is sufficient to prove the fact that FASnBr$_3$ nanocrystals are attached to the surface of the flexible Si-NWs. For the flexible Si-NWs, there is only an absorption peak at 895 nm in the whole absorption spectrum, and its absorption within the whole visible wavelength band is

relatively low [see Fig. 5(d)]. However, the obvious absorption peaks can be observed at 478 and 925 nm after the FASnBr$_3$ nanocrystals were spin-coated onto the surface of flexible Si-NWs. In addition, the introduction of FASnBr$_3$ nanocrystals not only effectively compensates for their absorption in the visible wavelength band, but also the formation of the Si-NWs/FASnBr$_3$ bulk-heterojunction mentioned above ensures the preparation for high-performance self-driven photodetectors.

It is well known that silicon nanowire arrays obtained by metal-assisted etching have a large number of defects. The MoO$_3$ layer with high stability is selected as the electron-blocking layer and protective layer during preparing the photodetectors [24], [25], and two kinds of self-driven photodetectors are fabricated on the very thin silicon substrates: 1) Si/Si-NWs/MoO$_3$/Au (device A) and 2) Si/[Si-NWs/FASnBr$_3$]/MoO$_3$/Au (device B). The schematic of the energy band levels for the Si-NWs/FASnBr$_3$ heterostructures before and after contacting as well as the photogenerated carriers' transportation within the photodetectors Si/Si-NWs/MoO$_3$/Au and Si/[Si-NWs/FASnBr$_3$]/MoO$_3$/Au are shown in Fig. 6. Fig. 6(a) shows a schematic of the energy bands of the FASnBr$_3$ nanocrystals and the flexible Si-NWs before their contacting. Herein, the FASnBr$_3$ nanocrystals and the flexible Si-NWs can form a type-I heterojunction after their contacting. As shown in Fig. 6(b), the photogenerated electrons will be retained in the conduction band, and the photogenerated holes will be retained in the valence band under the influence of the FASnBr$_3$ barrier (under 980 nm illumination). In addition, the photogenerated electrons and holes from FASnBr$_3$ will recombine at Si-NWs under 405 nm illumination [see Fig. 6(c)]. Thus, a MoO$_3$ layer is introduced into these photodetectors, and the schematics of these two self-driven photodetectors Si/Si-NWs/MoO$_3$/Au and Si/[Si-NWs/FASnBr$_3$]/MoO$_3$/Au under 980-illumination are shown in Fig. 6(d) and (e), respectively. In the above cases, photogenerated holes can be transported to the Au electrode via the hole-transporting MoO$_3$ layer. However, MoO$_3$ has a bandgap
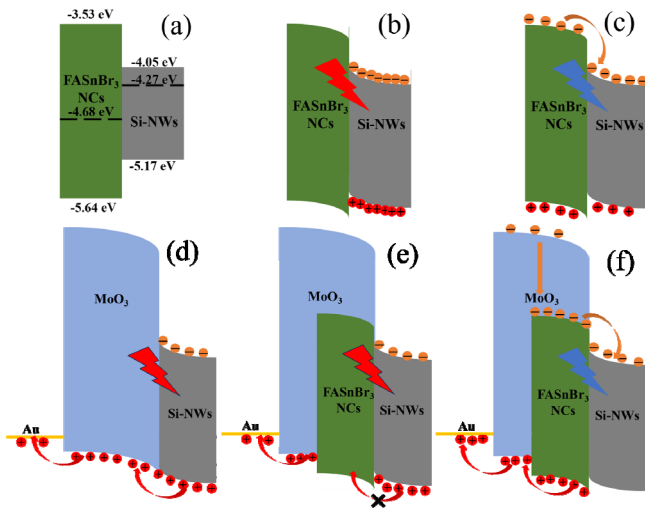
Fig. 6. (a) Band diagram of the Si-NWs/FASnBr$_3$ heterostructures before contacting. The schematic energy band diagram for electron-transporting mechanism within the Si-NWs/FASnBr$_3$ heterojunction under (b) 405 nm and (c) 980 nm illuminations. (d) Schematic energy band diagram for electron-transporting mechanism within the photodetector Si/Si-NWs/MoO$_3$/Au under 980 nm illumination. The schematic energy band diagram for electron-transporting mechanism within the photodetector Si/[Si-NWs/FASnBr$_3$]/MoO$_3$/Au under (e) 980 nm and (f) 405 nm illuminations. (The red and blue incident lights represent 980 and 405 nm illuminations, respectively.)
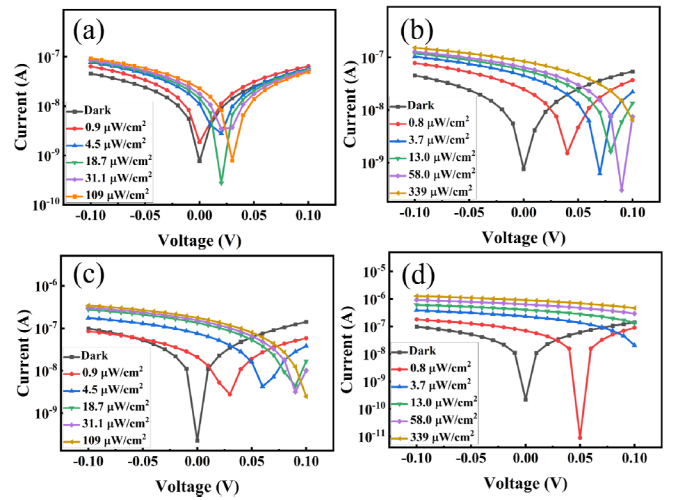

Fig. 7. I–V curves of photodetector Si/Si-NWs/MoO$_3$/Au under (a) 405 nm and (b) 980 nm illumination in different incident power intensities. The I–V curves of photodetector Si/[Si-NWs/FASnBr$_3$]/MoO$_3$/Au under (c) 405 nm and (d) 980 nm illumination in different incident power intensities.

of 3.0 eV, and thus, the incident wavelength of 405 nm illumination can be absorbed by the MoO$_3$ layer. Therefore, the photogenerated electrons and holes can be generated in the MoO$_3$ layer and then transport to the corresponding electrodes [see Fig. 6(f)].

In order to further verify the underlain mechanism between the photodetectors Si/Si-NWs/MoO$_3$/Au and Si/[Si-NWs/FASnBr$_3$]/MoO$_3$/Au, their performance under 405 and 980 nm illuminations, respectively, was measured. For photodetectors, it is important to further increase its photocurrent when its dark current was controlled. The dark current of photodetectors mainly originates from the injecting of carries through electrodes and defects within the active layer, such as component and structural defects, grain boundaries, and pinholes in the thin film [26]. On the one hand, these photodetectors were operated at zero bias, and thus, the number of carriers that are injected from the electrodes will be drastically reduced. On the other hand, the Si-NWs prepared by a silver-assisted chemical etching method suffer from a large number of defects. Therefore, photodetectors based on Si-NWs without passivation tend to show higher dark currents. In order to enhance the performance of the above photodetectors, the passivation engineering is necessary. However, FASnBr$_3$ nanocrystals cannot fully cover the nanowire surface to be a thin film. Therefore, the hole-transporting MoO$_3$ layer is selected and it is further attached to the surface of Si-NWs covered with FASnBr$_3$ nanocrystal layer. As one can see from Fig. 7(a) and (b), the dark current of the photodetector Si/Si-NWs/MoO$_3$/Au is 7.59 × 10^{-10} A at 0 V; meanwhile, its photocurrent gets relatively smaller under 405 and 980 nm illuminations. However, the dark current at zero bias just decreased from the original 7.59 × 10^{-10} to 2.42 × 10^{-10}

A after decorating FASnBr$_3$ nanocrystals onto the Si-NWs, as shown in Fig. 7(c) and (d). After the passivation of Si-NWs by FASnBr$_3$ nanocrystals and MoO$_3$, the defects of the above photodetectors were further suppressed; as a result, there is also a substantial decrease in the dark current of the above devices in the presence of the FASnBr$_3$ barrier. In addition, the photocurrent increased from the original 1.84 × 10^{-9} to 2.08 × 10^{-8} A, under 0.9 μW/cm^2 405 nm illumination at 0 V. The photocurrent increased from the original 2.49 × 10^{-8} to 6.99 × 10^{-8} A at 0 V under 0.8 μW/cm^2 980 nm illumination. As a result, the performance of these photodetectors has been enhanced greatly after the Si-NWs are decorated with FASnBr$_3$ nanocrystals.

To further investigate the performance of the above photodetectors, we fit their photocurrent by the following equation:

$$I_{ph} = k \cdot P_{opt}^{\alpha} \tag{3}$$

where $I_{ph} = I_p - I_d$, k is a constant, P_{opt} is the incident light intensity, and α represents the power law index. After the passivation of Si-NWs by FASnBr$_3$ nanocrystals, α increases from the original 0.287 to 0.360 under 405 nm illumination at 0 V, and α increases from the original 0.153 to 0.291 under 980 nm illumination at 0 V (see Fig. 8). Theoretically, the photocurrent will increase linearly with the incident illumination intensity, and however, the semiconductor material in the presence of a large number of defects and the trap states become recombination centers under illumination. Therefore, its photocurrent will reach saturation when the illumination intensity of incident light reaches a certain level. In a word, the photocurrent increases nonlinearly with incident illumination intensity.

In addition, the responsivity (R) and the specific detectivity (D^*) of the photodetectors were defined by the following
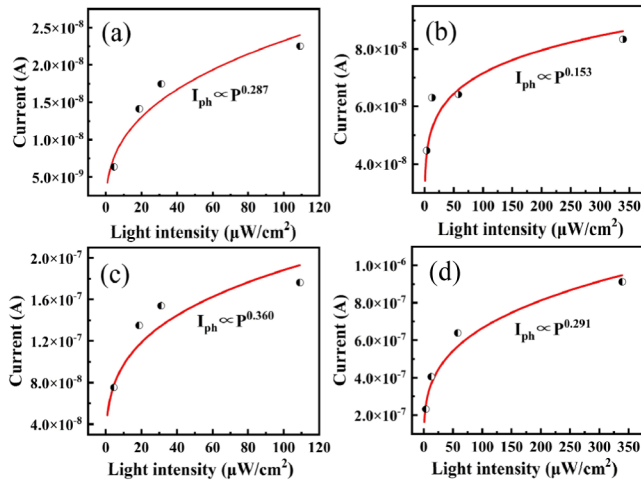
Fig. 8. Photocurrent from photodetector Si/Si-NWs/MoO$_3$/Au under (a) 405 nm and (b) 980 nm illuminations at zero bias. The photocurrent from photodetector Si/[Si-NWs/FASnBr$_3$]/MoO$_3$/Au under (c) 405 nm and (d) 980 nm illuminations at zero bias.

equations:

$$R = \frac{I_p - I_d}{P_{opt} \cdot A} \tag{4}$$

$$D^* = \frac{A^{1/2} \cdot R}{(2eI_d)^{1/2}} \tag{5}$$

where I_p is the photocurrent under illumination, I_d is the dark current, P_{opt} is the incident light intensity, A is the effective photosensitive area, and e is the elementary charge. As mentioned previously, the photocurrent of the photodetector increases nonlinearly with the incident illumination intensity, but its responsivity and specific detectivity decrease with increasing the incident light intensity. As shown in Fig. 9(a) and (b), the responsivity and specific detectivity of the photodetector Si/Si-NWs/MoO$_3$/Au are 0.00958 A/W and 2.18 × 10^{11} Jones, respectively, under 0.9 μW/cm^2 405 nm illumination at zero bias; meanwhile, the responsivity and the specific detectivity of the photodetector Si/[Si-NWs/FASnBr$_3$]/MoO$_3$/Au are 0.183 A/W and 7.65 × 10^{12} Jones, respectively. In Fig. 9(c) and (d), the responsivity and specific detectivity of the photodetector Si/Si-NWs/MoO$_3$/Au are 0.241 A/W and 5.47 × 10^{12} Jones, respectively, under 0.8 μW/cm^2 980 nm illumination at zero bias; meanwhile, the responsivity and the specific detectivity of the photodetector Si/[Si-NWs/FASnBr$_3$]/MoO$_3$/Au are 0.694 A/W and 2.90 × 10^{13} Jones, respectively. As a result, the above self-driven photodetectors in which the active layer is surface passivated with FASnBr$_3$ nanocrystals show enhanced performance greatly.

Furthermore, the $I-T$ curves of the self-driven photodetector Si/[Si-NWs/FASnBr$_3$]/MoO$_3$/Au at zero bias under 405 and 980 nm are shown in Fig. 10(a) and (d), respectively. As we know, the rising time (τ_r) is defined as the time required for the photocurrent increases from 10% to 90% of the maximum photocurrent, and the falling time (τ_f) is defined as the time required for the maximum photocurrent decreases from 90% to 10%. After calculating, we know that τ_r and τ_f are 92.416 and 58.984 ms, respectively, for the photodetector
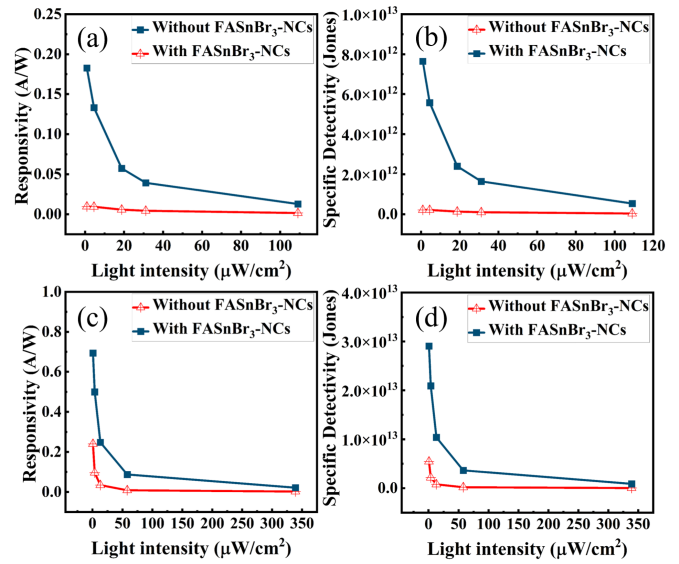

Fig. 9. (a) Responsivity and (b) specific detectivity of photodetectors Si/Si-NWs/MoO$_3$/Au and Si/[Si-NWs/FASnBr$_3$]/MoO$_3$/Au under 405 nm illumination. (c) Responsivity and (d) specific detectivity of photodetectors Si/Si-NWs/MoO$_3$/Au and Si/[Si-NWs/FASnBr$_3$]/MoO$_3$/Au under 980 nm illumination.
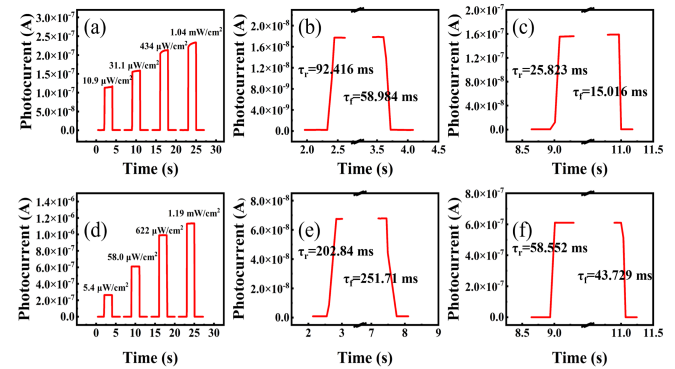

Fig. 10. $I-T$ curves of the photodetector Si/[Si-NWs/FASnBr$_3$]/MoO$_3$/Au under (a) 405 nm and (d) 980 nm illuminations at 0 V. The rising time (τ_r) and falling time (τ_f) for the photodetector Si/Si-NWs/MoO$_3$/Au under (b) 31.1 μW/cm^2 and 405 nm and (e) 58.0 μW/cm^2 980 nm illuminations at 0 V. The rising time (τ_r) and falling time (τ_f) for the photodetector Si/[Si-NWs/FASnBr$_3$]/MoO$_3$/Au under (c) 31.1 μW/cm^2 405 nm and (f) 58.0 μW/cm^2 980 nm illuminations at 0 V.

Si/Si-NWs/MoO$_3$/Au under 31.1 μW/cm^2 405 nm illumination [see Fig. 10(c)]. However, τ_r and τ_f increase to 202.84 and 251.71 ms, respectively, under 58.0 μW/cm^2 980 nm illumination [see Fig. 10(e)]. In addition, τ_r and τ_f are 25.823 and 28.016 ms, respectively, for the photodetector Si/[Si-NWs/FASnBr$_3$]/MoO$_3$/Au under 31.1 μW/cm^2 405 nm illumination [see Fig. 10(c)]. Also, τ_r and τ_f increase to 58.552 and 43.729 ms, respectively, under 58.0 μW/cm^2 980 nm illumination [see Fig. 10(f)]. From these data, one can see that the Si-NWs based self-driven photodetector Si/Si-NWs/MoO$_3$/Au shows a longer response time than that of the photodetector Si/[Si-NWs/FASnBr$_3$]/MoO$_3$/Au. Typically, the response time of the photodetector is related to the defects within its active layer. The response time of this photodetector can be greatly improved by surface passivating Si-NWs with

FASnBr$_3$ nanocrystals. In addition, we found that the response time of the self-driven photodetector Si/Si-NWs/MoO$_3$/Au under 405 nm illumination was much shorter than that under 980 nm illumination. Obviously, the main factor contributing to the above phenomenon is the introduction of MoO$_3$ layer. Actually, the incident illumination at 405 nm can be absorbed by MoO$_3$ [27] since MoO$_3$ has a bandgap of 3.0 eV. In addition, there is no barrier for photogenerated holes from MoO$_3$ to Au electrode under 405 nm irradiation, whereas there is a barrier for the photogenerated holes from Si-NWs to Au electrode under 980 nm irradiation. In addition, after surface passivating Si-NWs with FASnBr$_3$ nanocrystals, the photodetectors Si/[Si-NWs/FASnBr$_3$]/MoO$_3$/Au still show a quicker response under 405 nm illumination. Therefore, such a kind of high-performance flexible self-driven photodetectors will show promise for the subsequent development of wearable and intelligent devices by surface passivating Si-NWs with FASnBr$_3$ nanocrystals.

IV. CONCLUSION

In conclusion, we have presented enhanced-performance self-driven photodetectors based on flexible silicon nanowire (Si-NW) array, i.e., Si/[Si-NWs/FASnBr$_3$]/MoO$_3$/Au, in which the active layer was surface passivated with tin-based perovskites. The responsivity and specific detectivity of the photodetectors Si/Si-NWs/MoO$_3$/Au increase from 0.00958 A/W and 2.18×10^{11} Jones to 0.183 A/W and 7.65×10^{12} Jones under 0.9 μW/cm^2 405 nm illumination at zero bias, respectively. After surface passivating, the corresponding responsivity and specific detectivity of the photodetector Si/[Si-NWs/FASnBr$_3$]/MoO$_3$/Au increase from 0.241 A/W and 5.47×10^{12} Jones to 0.694 A/W and 2.90×10^{13} Jones under 0.8 μW/cm^2 980 nm illumination at zero bias, respectively. In addition, the response time was reduced after the active layer (i.e., Si-NWs) was surface passivated with FASnBr$_3$ nanocrystals. Therefore, it provides a feasible way for high-performance flexible self-driven photodetectors for the subsequent development of wearable and intelligent devices.

REFERENCES

[1] Y. Ning, Z. Zhang, F. Teng, and X. Fang, "Novel transparent and self-powered UV photodetector based on crossed ZnO nanofiber array homojunction," *Small*, vol. 14, no. 13, Mar. 2018, Art. no. 1703754.

[2] J. Li et al., "Tuning the properties of a self-powered UV photodetector based on ZnO and poly(3,4-ethylenedioxythiophene): Poly(styrenesulfonate) by hydrogen annealing of ZnO nanorod arrays," *Thin Solid Films*, vol. 628, pp. 101–106, Apr. 2017.

[3] C. Zhao et al., "Self-powered, high-speed and visible-near infrared response of MoO$_{3-x}$/n-Si heterojunction photodetector with enhanced performance by interfacial engineering," *ACS Appl. Mater. Interfaces*, vol. 7, no. 46, pp. 25981–258990, 2015.

[4] I. M. Asuo, D. Banerjee, A. Pignolet, R. Nechache, and S. G. Cloutier, "Perovskite/silicon-nanowire-based hybrid heterojunctions for fast and broadband photodetectors," *Phys. Status Solidi (RRL) Rapid Res. Lett.*, vol. 15, no. 4, Apr. 2021, Art. no. 2000537.

[5] X.-X. Yu, H. Yin, H.-X. Li, H. Zhao, C. Li, and M.-Q. Zhu, "A novel high-performance self-powered UV-vis-NIR photodetector based on a CdS nanorod array/reduced graphene oxide film heterojunction and its piezo-phototronic regulation," *J. Mater. Chem. C*, vol. 6, no. 3, pp. 630–636, 2018.

[6] F. Cao, L. Meng, M. Wang, W. Tian, and L. Li, "Gradient energy band driven high-performance self-powered perovskite/CdS photodetector," *Adv. Mater.*, vol. 31, no. 12, Mar. 2019, Art. no. 1806725.

[7] Q. Hong et al., "Self-powered ultrafast broadband photodetector based on p-n heterojunctions of CuO/Si nanowire array," *ACS Appl. Mater. Interfaces*, vol. 6, no. 23, pp. 20887–208894, 2014.

[8] L. Rao et al., "Polar-Solvent-Free synthesis of highly photoluminescent and stable CsPbBr$_3$ nanocrystals with controlled shape and size by ultrasonication," *Chem. Mater.*, vol. 31, no. 2, pp. 365–375, Jan. 2019.

[9] J. Liu et al., "Silicon/perovskite core-shell heterojunctions with light-trapping effect for sensitive self-driven near-infrared photodetectors," *ACS Appl. Mater. Interfaces*, vol. 10, no. 33, pp. 27850–27857, 2018.

[10] C. Xu et al., "Bias-selectable Si nanowires/PbS nanocrystalline film n–n heterojunction for NIR/SWIR dual-band photodetection," *Adv. Funct. Mater.*, vol. 33, no. 28, Jul. 2023, Art. no. 2214996.

[11] X. Ma et al., "A flexible plasmonic-membrane-enhanced broadband tin-based perovskite photodetector," *Nano Lett.*, vol. 21, no. 21, pp. 9195–9202, Nov. 2021.

[12] L. Dai et al., "Slow carrier relaxation in tin-based perovskite nanocrystals," *Nature Photon.*, vol. 15, no. 9, pp. 696–702, Sep. 2021.

[13] Z. Zhang et al., "High-stability lead-free tin(II)-perovskites by A-site cation engineering and surface passivating engineering for high-performance hybrid bulk-heterojunction photodetectors," *J. Alloys Compounds*, vol. 960, Oct. 2023, Art. no. 170867.

[14] Y. Xu, H. Shen, Z. Yue, S. Wang, Q. Zhao, and Z. Wang, "An ultra-flexible silicon substrate with light-trapping structures: The application for visible-NIR photodetectors," *Surf. Interfaces*, vol. 33, Oct. 2022, Art. no. 102288.

[15] Y. Wu et al., "Silicon nanowires array capped with two shells as light-absorption antenna for self-driven broadband photodetectors," *Appl. Phys. Lett.*, vol. 123, no. 5, Jul. 2023, Art. no. 053301.

[16] C. Ferrara et al., "Wide band-gap tuning in Sn-based hybrid perovskites through cation replacement: The FA1-xMAxSnBr3 mixed system," *J. Mater. Chem. A*, vol. 5, no. 19, pp. 9391–9395, 2017.

[17] P. Ambra et al., "Exploring the limits of three-dimensional perovskites: The case of FAPb1-xSnxBr3," *ACS Energy Lett.*, vol. 3, no. 6, pp. 1353–1359, 2018.

[18] A. F. Akbulatov et al., "Comparative intrinsic thermal and photochemical stability of Sn(II) complex halides as next-generation materials for lead-free perovskite solar cells," *J. Phys. Chem. C*, vol. 123, no. 44, pp. 26862–26869, Nov. 2019.

[19] H. Wang et al., "Transport in a single self-doped nanocrystal," *ACS Nano*, vol. 11, no. 2, pp. 1222–1229, Feb. 2017.

[20] B. Huo et al., "Amino-mediated anchoring of FAPbBr$_3$ perovskite quantum dots on silica spheres for efficient visible light photocatalytic NO removal," *Chem. Eng. J.*, vol. 406, Feb. 2021, Art. no. 126740.

[21] K. Hills-Kimball, Y. Nagaoka, C. Cao, E. Chaykovsky, and O. Chen, "Synthesis of formamidinium lead halide perovskite nanocrystals through solid–liquid–solid cation exchange," *J. Mater. Chem. C*, vol. 5, no. 23, pp. 5680–5684, 2017.

[22] H. J. Jeong et al., "Quasi-2D halide perovskite memory device formed by acid-base binary ligand solution composed of oleylamine and oleic acid," *ACS Appl. Mater. Interfaces*, vol. 13, no. 34, pp. 40891–40900, 2021.

[23] G. Shao, "Work function and electron affinity of semiconductors: Doping effect and complication due to Fermi level pinning," *ENERGY Environ. Mater.*, vol. 4, no. 3, pp. 273–276, Jul. 2021.

[24] A. Mondal and Y. A. K. Reddy, "Enhanced photodetector performance of nanostructured MoO$_{3-x}$ thin films by inert annealing," *IEEE Sensors J.*, vol. 24, no. 3, pp. 2726–2733, Feb. 2024.

[25] A. Mondal and Y. A. K. Reddy, "Influence of oxygen partial pressure on the performance of MoO$_3$-based ultraviolet photodetectors," *Surf. Interfaces*, vol. 41, Oct. 2023, Art. no. 103179.

[26] R. Ollearo et al., "Ultralow dark current in near-infrared perovskite photodiodes by reducing charge injection and interfacial charge generation," *Nature Commun.*, vol. 12, no. 1, p. 7277, Dec. 2021.

[27] J. Song, X. Ni, D. Zhang, and H. Zheng, "Fabrication and photoluminescence properties of hexagonal MoO$_3$ rods," *Solid State Sci.*, vol. 8, no. 10, pp. 1164–1167, Oct. 2006.

Zhenheng Zhang received the B.S. degree from Changzhi University, Changzhi, China, in 2017. He is currently pursuing the Ph.D. degree with Beijing Institute of Technology, Beijing, China.

His current research interests include quantum dots, perovskite, and photodetectors.
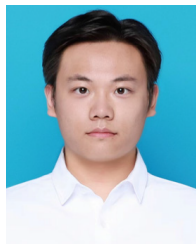
Haiyuan Xin received the B.S. degree from Changchun University of Science and Technology, Changchun, China, in 2021. He is currently pursuing the M.S. degree with Beijing Institute of Technology, Beijing, China.

His current research interests include silicon nanowires, graphene, and photodetectors.

Ying Wang received the B.S. degree from the University of Science and Technology Beijing, Beijing, China, in 2021. She is currently pursuing the M.S. degree with Beijing Institute of Technology, Beijing.

Her current research interests include quantum dots, perovskite, and photodetectors.

Shengyi Yang received the Ph.D. degree from Beijing Jiaotong University, Beijing, China, in 2001.

He is a Professor at Beijing Institute of Technology, Beijing. His current research interests include colloidal quantum dots (CQDs) based photodetectors, solar cells, and light-emitting diodes. His team is focusing on novel nanomaterials and its optoelectronic devices.

Yurong Jiang received the Ph.D. degree from Wuhan Institute of Physics and Mathematics, Chinese Academy of Sciences, Beijing, China, in 2001.

She is an Associate Professor with Beijing Institute of Technology, Beijing. Her current research interests include optical thin films, photonic crystals, and flat-panel displays.

Zhenhua Ge received the B.S. degree from Changshu Institute of Technology, Changzhi, China, in 2018, and the M.S. degree from Tianjin University of Technology, Tianjin, China, in 2021. He is currently pursuing the Ph.D. degree with Beijing Institute of Technology, Beijing, China.

His current research interests include quantum dots, photodetectors, and upconverters.

Bingsuo Zou received the Ph.D. degree from Jilin University, Jilin, China, in 1991.

He is a Professor with Guangxi University, Nanning, China. His current research interests include nanophotonics, optoelectronic materials and devices, physics of optoelectronic materials, laser spectroscopy, and nonlinear optics.